



## OPEN ACCESS

EDITED BY  
Raphaël Turcotte,  
Albert Einstein College of Medicine,  
United States

REVIEWED BY  
Carlas Smith,  
Delft University of Technology, Netherlands  
Fei Xia,  
École Normale Supérieure, France

\*CORRESPONDENCE  
Luke J. Mortensen  
✉ luke.mortensen@uga.edu  
Peter A. Kner  
✉ kner@uga.edu

SPECIALTY SECTION  
This article was submitted to  
Brain Imaging Methods,  
a section of the journal  
Frontiers in Neuroimaging

RECEIVED 01 June 2022  
ACCEPTED 09 January 2023  
PUBLISHED 16 February 2023

CITATION  
Zheng T, Liversage AR, Tehrani KF, Call JA,  
Kner PA and Mortensen LJ (2023) Imaging  
mitochondria through bone in live mice using  
two-photon fluorescence microscopy with  
adaptive optics. *Front. Neuroimaging* 2:959601.  
doi: 10.3389/fnimg.2023.959601

COPYRIGHT  
© 2023 Zheng, Liversage, Tehrani, Call, Kner  
and Mortensen. This is an open-access article  
distributed under the terms of the [Creative  
Commons Attribution License \(CC BY\)](https://creativecommons.org/licenses/by/4.0/). The use,  
distribution or reproduction in other forums is  
permitted, provided the original author(s) and  
the copyright owner(s) are credited and that  
the original publication in this journal is cited, in  
accordance with accepted academic practice.  
No use, distribution or reproduction is  
permitted which does not comply with these  
terms.

# Imaging mitochondria through bone in live mice using two-photon fluorescence microscopy with adaptive optics

Tianyi Zheng<sup>1</sup>, Adrian R. Liversage<sup>2</sup>, Kayvan F. Tehrani<sup>3</sup>,  
Jarrod A. Call<sup>4</sup>, Peter A. Kner<sup>1\*</sup> and Luke J. Mortensen<sup>2,5\*</sup>

<sup>1</sup>School of Electrical and Computer Engineering, University of Georgia, Athens, GA, United States, <sup>2</sup>School of Chemical, Materials and Biomedical Engineering, University of Georgia, Athens, GA, United States, <sup>3</sup>Biophotonics Imaging Laboratory, The University of Illinois Urbana-Champaign, Urbana, IL, United States, <sup>4</sup>Department of Physiology and Pharmacology, University of Georgia, Athens, GA, United States, <sup>5</sup>Regenerative Bioscience Center, Rhodes Center for ADS, University of Georgia, Athens, GA, United States

**Introduction:** Mitochondria are extremely important organelles in the regulation of bone marrow and brain activity. However, live imaging of these subcellular features with high resolution in scattering tissues like brain or bone has proven challenging.

**Methods:** In this study, we developed a two-photon fluorescence microscope with adaptive optics (TPFM-AO) for high-resolution imaging, which uses a home-built Shack-Hartmann wavefront sensor (SHWFS) to correct system aberrations and a sensorless approach for correcting low order tissue aberrations.

**Results:** Using AO increases the fluorescence intensity of the point spread function (PSF) and achieves fast imaging of subcellular organelles with 400 nm resolution through 85  $\mu\text{m}$  of highly scattering tissue. We achieved  $\sim 1.55\times$ ,  $\sim 3.58\times$ , and  $\sim 1.77\times$  intensity increases using AO, and a reduction of the PSF width by  $\sim 0.83\times$ ,  $\sim 0.74\times$ , and  $\sim 0.9\times$  at the depths of 0, 50  $\mu\text{m}$  and 85  $\mu\text{m}$  in living mouse bone marrow respectively, allowing us to characterize mitochondrial health and the survival of functioning cells with a field of view of 67.5  $\times$  67.5  $\mu\text{m}$ . We also investigate the role of initial signal and background levels in sample correction quality by varying the laser power and camera exposure time and develop an intensity-based criteria for sample correction.

**Discussion:** This study demonstrates a promising tool for imaging of mitochondria and other organelles in optically distorting biological environments, which could facilitate the study of a variety of diseases connected to mitochondrial morphology and activity in a range of biological tissues.

## KEYWORDS

two-photon fluorescence microscopy, aberration, adaptive optics, mitochondria, mouse cranial bone

## 1. Introduction

Mitochondria are intracellular organelles with 0.5 to 10  $\mu\text{m}$  diameter that drive energy production processes through the respiratory chain by oxidative phosphorylation (Siesjo, 1978; Siegel et al., 1981). They play a fundamental role in numerous physiological processes of critical importance in tissue homeostasis and repair, such as cell differentiation (Folmes et al., 2012), apoptosis (Miao et al., 2014), signal transduction (Xu et al., 2016), reactive oxygen species generation (Murphy, 2009), and maintenance of healthy organ function (Gropman, 2004). Their function is highly dynamic and reflected in mitochondrial network structure, and imaging technologies are therefore essential to understand physiological mitochondrial processes in health and disease. High energy requirement tissues such as the brain and bone marrow are especially dependent on carefully orchestrated mitochondrial maintenance and activity.

Over the last decades, the evaluation of live tissue dynamics at cellular resolution using intravital imaging has transformed the biological understanding of organ function at a single cell level. In the bone, this has significantly advanced the scientific understanding of vascular dynamics, stem cell biology, and bone homeostasis and regeneration (Lo Celso et al., 2009; Spencer et al., 2014; Itkin et al., 2016; Wilk et al., 2017; Christodoulou et al., 2020). In the brain, intravital imaging has generated unique insight into brain circuitry and processing, brain cancer, brain trauma, and degenerative diseases (Andermann and Kerlin, 2010; Shih et al., 2012; Ricard, 2014; Yang et al., 2018; Calvo-Rodriguez et al., 2019; Chen et al., 2019; Hu et al., 2021). However, one of the most serious obstacles to imaging is the poor penetration depth of intravital optical microscopy. Single photon imaging with confocal detection is a common approach that uses visible light for fluorescence excitation (400–650 nm), where light penetration is attenuated by absorption and scattering of skull bone and tissues (Shi et al., 2016; Wang et al., 2018). To extend imaging depth, high energy pulses of near-IR excitation light (760–1,080 nm) can be tightly focused to create a non-linear two-photon absorption process using standard fluorophores. Two-photon imaging extends the attainable imaging depth to 500  $\mu\text{m}$ –1 mm of brain tissue and up to  $\sim 150 \mu\text{m}$  in highly scattering bone (Denk and Strickler, 1990; Hell, 1992; Xu, 1996; Callis, 1997; Diaspro et al., 2006; Sinfeld et al., 2015). However, non-homogeneous wave propagation through these irregular and highly distorting turbid media induces high magnitude phase deviations in the wavefront (Tehrani et al., 2017a) that dramatically reduce image resolution even at moderate depths. Therefore, cranial windows and skull-thinning methods are commonly adopted to improve optical access (Jeong and Tsai, 2013; Yang et al., 2013; Chen et al., 2021). However, the surgery increases the risk of tissue inflammation and may cause stress that could alter biological function in the target tissues (Li and Baran, 2014).

One way to overcome this challenge is with adaptive optics (AO). An AO system typically consists of a deformable mirror conjugated to the back pupil plane of a microscope, and either wavefront sensor or image-based sensorless wavefront estimation methods to correct aberrations and improve the resolution, which can improve *in vivo* imaging in animal models (Albert et al., 2000; Wright et al., 2005; Rueckel and Mack-Bucher, 2006; Débarre et al., 2009; Tao et al., 2013a; Kong, 2015a,b; Wang et al., 2015; Kong and Tang, 2016). Wavefront sensor approaches include Shack–Hartmann wavefront sensors with auto-fluorescent or near-IR guide stars (Tao et al., 2013a; Wang et al., 2015), coherence gated wavefront sensing (Rueckel and Mack-Bucher, 2006), and image-based methods that use information from acquired images to remove wavefront distortions (Marsh and Burns, 2003; Débarre et al., 2009; Kong, 2015a,b; Kong and Tang, 2016). Wavefront sensorless approaches usually estimate an initial error and through an iterative scheme converge to an optimized solution based on intensity metrics (Albert et al., 2000; Wright et al., 2005; Booth, 2006). Recently, non-linear guide stars with Shack–Hartmann measurements of wavefront aberrations have yielded an accurate measurement of low-order tissue aberrations that proves to be useful to extend imaging depth in biological samples but require long integration times and has a small effective field of view (Aviles-Espinosa et al., 2011; Tao et al., 2013b). In an alternative wavefront sensorless approach using rapid anisotropic aberration correction, the adaptive correction element was conjugated to the turbid layer instead of the focus, with the goal of increasing the size of the

isoplanatic patch (Park and Sun, 2015). Our bone marrow imaging occurs within an extended scattering layer, so such an approach is not appropriate.

In this study, we calculate and correct both the system aberration and the sample aberrations caused by mouse cranial bone and brain tissue to improve imaging for dynamic mitochondria localization. We demonstrate that low-order aberration correction provides a significant improvement when imaging through the bone into the bone marrow. We first compensate for the aberrations of our microscope system using a sensor-based AO algorithm, and then we compensate for the aberrations of mouse cranial bone by using a Zernike-mode-based sensorless AO algorithm because it requires comparatively less signal to optimize and create an improved wavefront profile. We use our two-photon fluorescence microscope with adaptive optics to image mitochondria in mouse cranial bone marrow and brain. We also find and evaluate the threshold and performance for intensity-based sample correction. This work shows that after AO correction, the fluorescence intensity of the point spread function (PSF) is improved, and the resolution of images is significantly improved when imaging through intact mouse cranial bone into the bone marrow, allowing us to characterize mitochondrial health and dynamics of functioning cells deep in tissue.

## 2. Methods

### 2.1. Preparation of fluorescent beads stack in gel

A total of 200nm yellow-green, fluorescent beads (ThermoFisher Scientific F8811) were diluted to a ratio of 1:200 in 2.0% agarose. Then, 0.2 grams of agarose powder (Bio-Rad, Certified Molecular Biology Agarose 1613101) were added to 10 milliliters of DI (Deionization) water to make the mass concentration 2.0%. Next, the agarose solution was heated in a microwave for intervals of 45 s. This process was continued until the agarose became a gel mixture. After 1–2 min passed for the agarose gel to cool down to a safe handling temperature, the agarose gel was ready to hold the beads in place for imaging analysis. In total, 2.0 ml of beads were added to 400 ml of agarose to achieve the 1:200 ratio. After drying completely, the Petri dish was then placed on the stage of the TPFM-AO system and DI water was added for imaging with the water dipping objective.

### 2.2. Mouse imaging

For mouse intravital imaging, we used a transgenic mouse model ubiquitously expressing mitochondrial-targeted Dendra2 green monomeric fluorescent protein (Jackson Laboratory, #018385) as previously described (Pham et al., 2012; Southern et al., 2019). The mouse was initially anesthetized using 4% isoflurane (100 ml/min oxygen flow) and restrained using a 3D printed stereotaxic holder. The holder is similar to those used in previously published works by several groups when studying cell dynamics in the brain and skull (Fried et al., 2001; Lo Celso et al., 2009; Leuschner et al., 2015; Turcotte et al., 2017; Tehrani et al., 2019b) and serves to

secure and stabilize the mouse skull while reducing mechanical coupling with the trunk of the body so that breathing movement artifacts are reduced. Five minutes before making an incision, 50  $\mu\text{l}$  of 0.25% bupivacaine was locally applied as analgesia. An incision was made on the scalp from between the eyes toward both ears to make a flap. The periosteum layer was removed, and the area of imaging was cleaned using a cotton swab; immediately sterile phosphate buffered saline (PBS) was applied to the incision site. The animal was placed under the microscope objective and sterile PBS was added to fill the gap between the skull and the objective lens. The rate of isoflurane was then reduced to 1.4% during imaging. For vasculature imaging, a 20  $\mu\text{l}$  dose of 70 kDa rhodamine-B dextran (Nanocs) was administered through retro-orbital injection before making an incision. After the intravital imaging session, mice were euthanized using  $\text{CO}_2$  and cervical dislocation. Immediately after sacrifice, the brain was extracted and mounted in a Petri dish using 2.0% agarose for mitochondrial imaging. All animal procedures and experiments were approved by the UGA Institutional Animal Care and Use Committee (IACUC).

### 2.3. Optical setup

A schematic of the adaptive optics two-photon fluorescence microscopy (AO-TPFM) system is shown in Figure 1, based on our previously published work (Tehrani et al., 2017b, 2021). The optical setup consists of a Chameleon Ti:Sapphire laser producing 680 to 1,080 nm 137 fs pulses of energy, with power at the source modulated using a half-waveplate and a polarizing beam splitter. The laser beam is recollimated and passed through a Pockels cell (Conoptics) for rapid intensity modulation during imaging. The beam is then expanded using a telescope with a pinhole in the focus to create a more uniformly Gaussian beam profile. The Pockels cell is used to block the beam during flyback, as well as correct beam intensity for the resonant scanner. The deformable mirror (DM, Alpao DM97-15) placed conjugate to the back pupil plane has a continuous face sheet and 97 actuators and is used for low-order AO wavefront correction. The DM is inserted into the beam path with two optical relay systems. Beam scanning is done by a Sutter instrument MDR-R box that houses a fast resonant galvo and a slow galvo scanner for horizontal and vertical sweeping, respectively. Both scanners are from Cambridge technology and are placed very close to each other to reduce astigmatism, with heatsinks. The scanned beam is relayed using two achromatic doublets—serving as the scanning and tube lenses, respectively—to the  $60 \times 1.00$  NA water immersion objective lens (Nikon, MRD07620). The back-propagated emission light from the sample is separated from the excitation light using a dichroic mirror DiM<sub>1</sub> (Semrock FF705-Di01) and sent to an sCMOS camera (ANDOR, Zyla Scientific CMOS) which is used to look at the PSF shape or separated with a dichroic mirror DiM<sub>2</sub> (Semrock FF705-Di01) and sent to the photon multiplier tubes (PMT) from Hamamatsu (H10770-40). DiM<sub>3-4</sub> (Semrock FF552-Di02, and FF409-Di03-25\*36) and filters F2-4 (Semrock 571/72 nm, 509/22 nm, and 390/18 nm) were used to separate each spectral channel to capture signals from two photon fluorescence (TPF), green fluorescent protein (GFP), and second

harmonic generation (SHG) of collagen, respectively. A home-built Shack-Hartmann wavefront sensor (SHWFS) was used, with a LabVIEW-based control and measurement software to measure the total system aberrations (red arrow shows beam direction) just before the objective lens (Figure 2A). Another LabVIEW-based control and measurement software was used for full AO correction. The MATLAB<sup>®</sup>-based open-source software, Scanimage (Pologruto and Sabatini, 2003) was employed to control the microscope after the correction.

### 2.4. Sensor-based system aberrations

Before measuring and correcting the aberrations of the biological samples, we first compensated for system aberrations using a sensor-based AO algorithm. The lenslet array creates spots in the image whose displacement versus an internal reference guidestar allows calculation of wavefront distortions (Figure 2B).

We use Eq. (1) to decompose the calculated wavefront into the Zernike modes (Zhao, 2007):

$$c_i = \frac{1}{\pi} \int_0^1 \int_0^{2\pi} \psi_i(\rho, \theta) Z_i(\rho, \theta) \rho d\theta d\rho, (1)$$

where  $Z$  is the Zernike mode of order  $i$  and  $c_i$  is the coefficient of the mode  $Z_i$ . Equation (1) yields a complete Zernike coefficient set that could be applied to a DM for correction. We take modes 5 to 37 [using Noll's ordering (Noll, 1976) of the Zernike modes, up to order 4] into consideration because these modes can be corrected by the DM. To find the corrected wavefront shape, we do a summation such that constructed phase equals

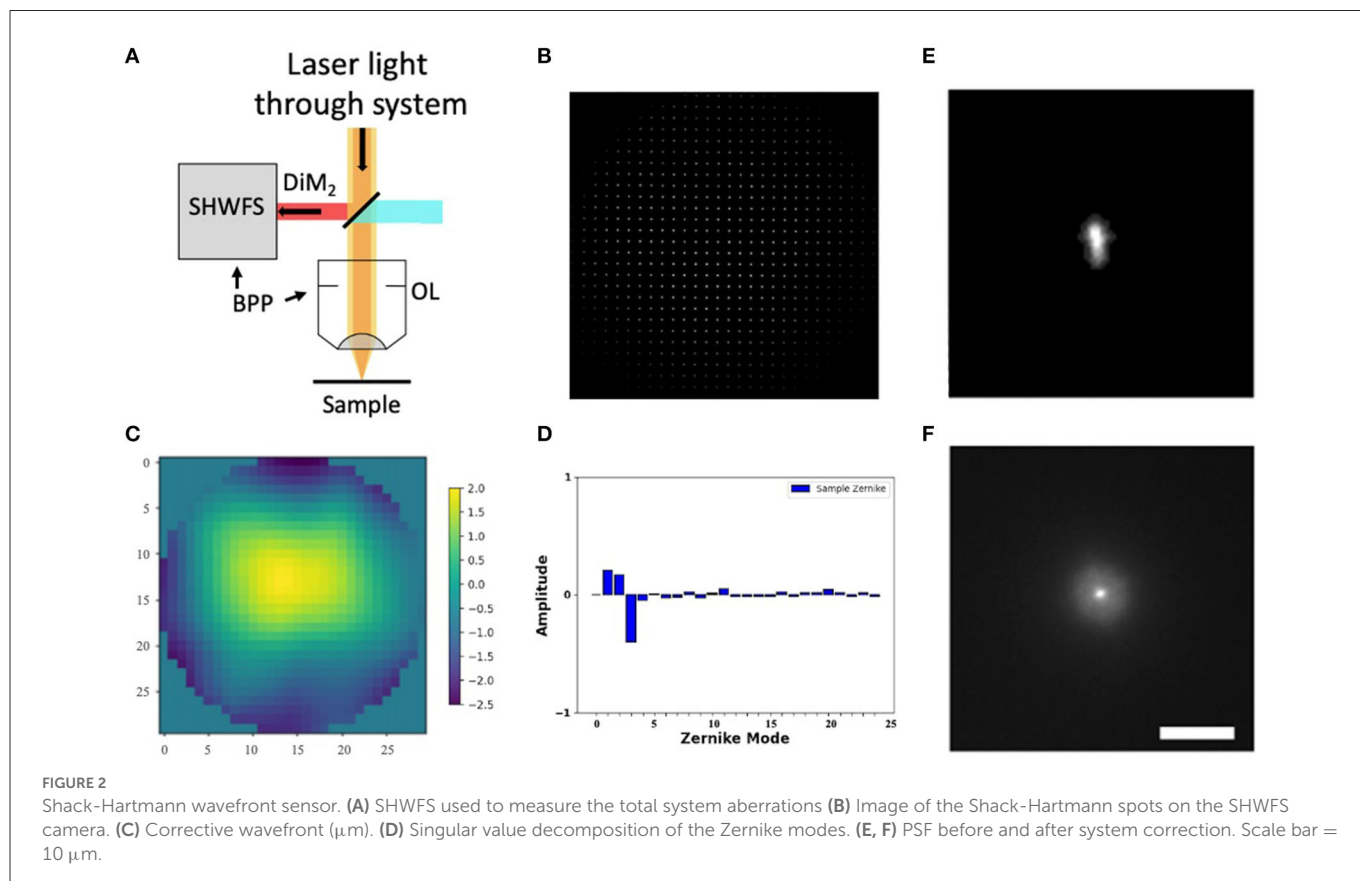
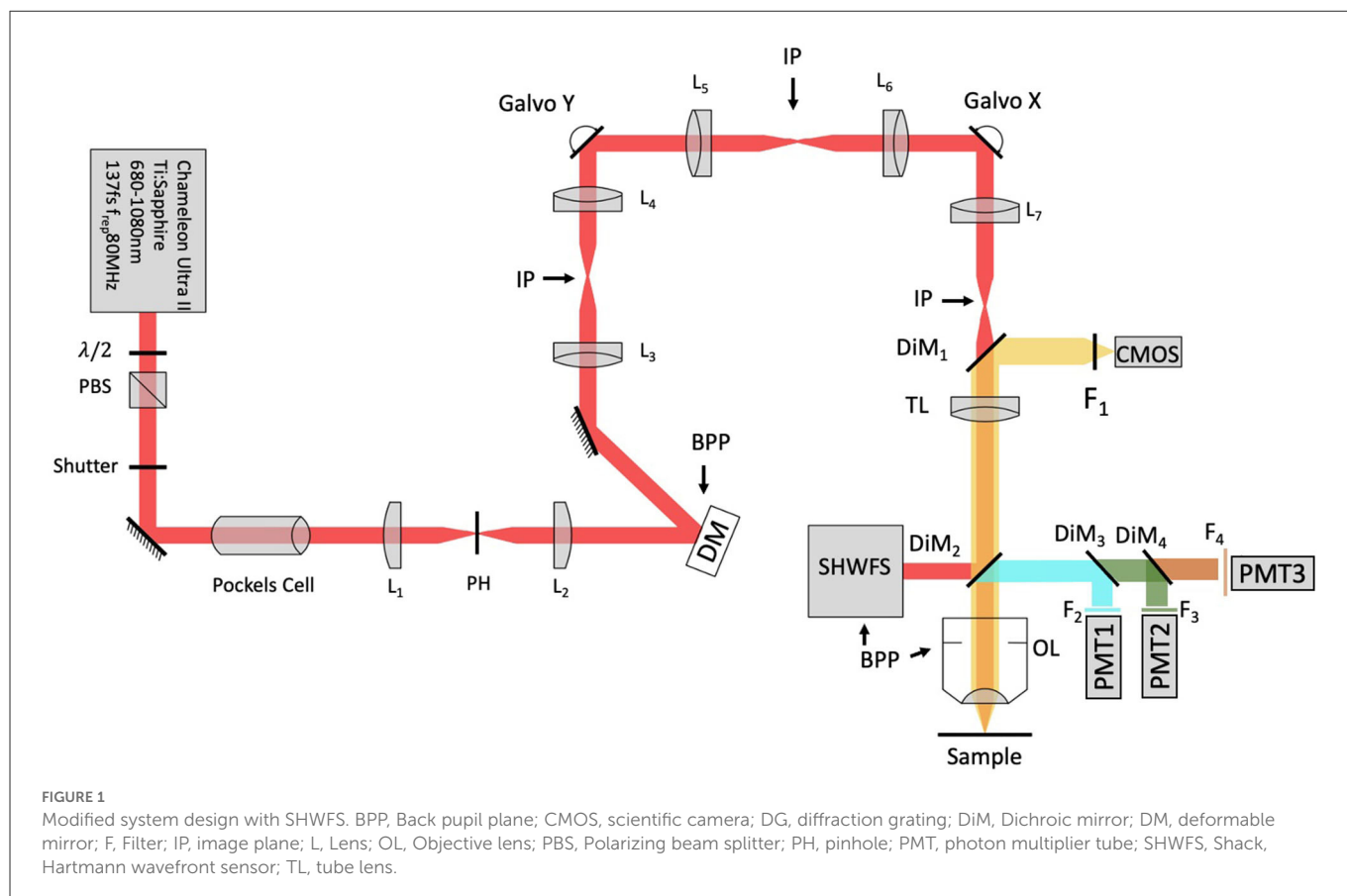
$$\psi_c(\rho, \theta) = \exp\left(-j \frac{2\pi}{\lambda} \sum_i c_i Z_i(\rho, \theta)\right) (2)$$

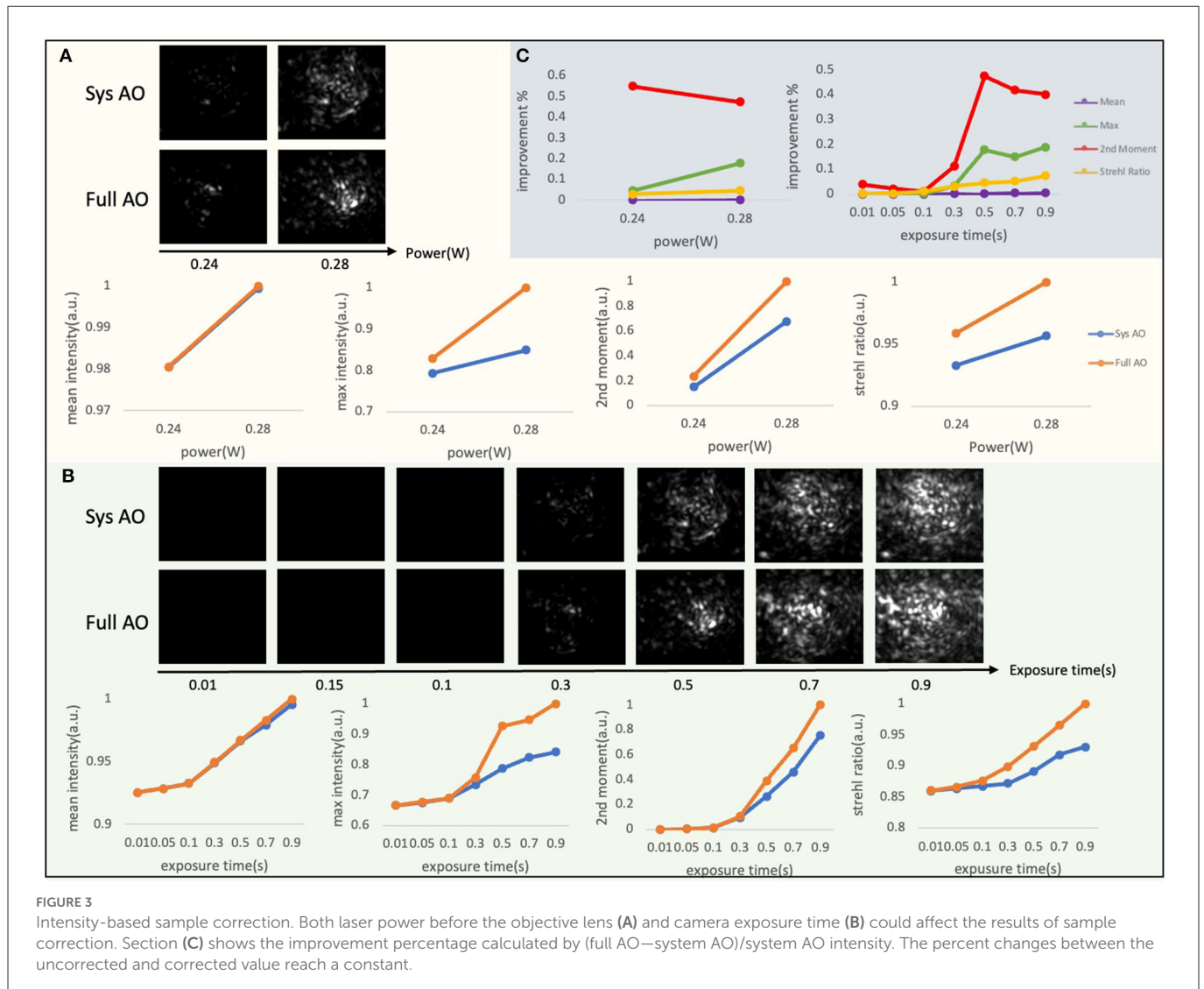
The root-mean-square (RMS) wavefront error that is corrected by the Zernike modes 4 to 37 (piston, tip, and tilt are not included) is calculated by  $\sigma = [\sum_i c_i^2]^{1/2}$ .

We perform one DM correction at each focal plane by scanning for a fluorescent signal and then optimizing the wavefront (Tehrani et al., 2019a). The wavefront of our excitation beam shows <2 waves of distortion, with Zernike decomposition of the wavefront identifying the strongest contributions from tip ( $Z_2$ ), tilt ( $Z_3$ ), and defocus ( $Z_4$ ) (Figures 2C, D). After applying the Shack-Hartmann wavefront correction, the PSF in the sample plane has a near diffraction-limited Gaussian shape (FWHM = 350 nm).

### 2.5. Sensorless sample aberration correction based on sum or max intensity

Wavefront aberrations are the difference in phase or optical path length from the ideal (e.g., spherical, or planar) form Neil et al. (2000), which can be caused by light propagation through an inhomogeneous medium like biological tissue. According to





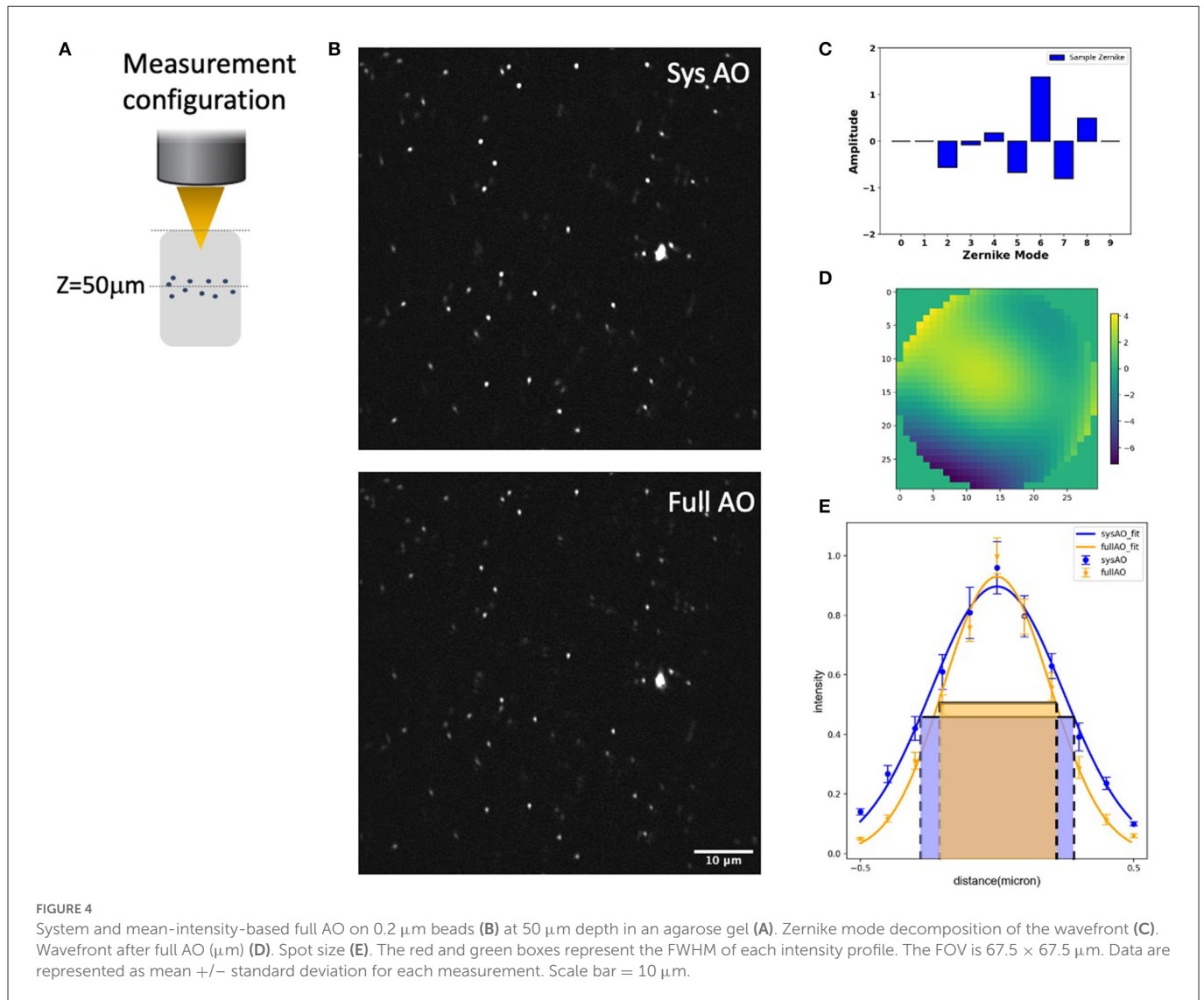
the Zernike mode equation, different combinations of the Zernike coefficients in a phase distribution at the back-pupil plane can alter the point spread function at the focal plane. If used to reconstruct the wavefront phase distribution with proper Zernike modes and coefficients by a DM placed conjugate to the back-pupil plane, this principle can compensate for the aberrations induced by tissue.

Sensorless AO uses the signal obtained with the microscope as an input for an algorithm that estimates the optical aberrations present in the system. Our implementation of sensorless AO is depicted in the flowchart in [Supplementary Figure S1](#). A series of PSFs is acquired with different Zernike aberration modes applied to a DM conjugate with the back pupil plane. To determine the optimal value for each Zernike mode, different values of aberration are applied to the DM. We evaluated 10 or 15 orders of Zernike modes (tip, tilt, and defocus excluded), which in our preliminary experiments using 10 or 15 modes for correction provided 90% of the enhancement found when including higher order modes. An image quality metric (e.g., max intensity) is then selected and evaluated for each image. Then a parabolic function is fitted to the measured points and the mode coefficient corresponding

to the estimated peak is applied as the correction. Subsequent modes are corrected in a similar manner to achieve convergence of the wavefront.

## 2.6. Sample correction parameter selection

During preliminary aberration correction experiments, we observed that the degree of enhancement achieved in sensorless sample correction has a dependence on the initial intensity conditions in low signal environments. Since a low starting signal is common when attempting to use AO, we explored the sensitivity of our correction strategy to different background noise and signal levels by modulating the laser power before the objective lens ([Figure 3A](#)) and the camera exposure time ([Figure 3B](#)). These measures both strongly influence the signal to background ratio of the PSF images used in the sample correction for a GFP mouse skull. We used two power levels at the sample, a commonly used average power on the sample for imaging 50–100  $\mu\text{m}$  deep in tissue, and the maximum average power that we experimentally observed not to cause visible



damage to the sample within our image acquisition time; and a range of integration times for each Zernike mode measure from 10 ms to 1 s. At each condition, we evaluated several measures of PSF quality, including the mean intensity, max intensity, second moment, and Strehl ratio. To calculate the second moment, the  $k$ -th central moment of a data sample is defined as:  $m_k = \frac{1}{n} \sum_{i=1}^n (x_i - \bar{x})^k$ , where  $n$  is the number of samples and  $\bar{x}$  is the mean. The Strehl ratio is defined as  $S = e^{-\frac{4\pi^2\sigma^2}{\lambda^2}}$ , where  $\sigma$  is the root mean square deviation of the wavefront,  $\lambda$  is the wavelength. In our situation, the experimental Strehl ratio is defined as the ratio of the peak aberrated image intensity from a point source compared to the maximum attainable intensity using an ideal optical system limited only by diffraction over the system's aperture.

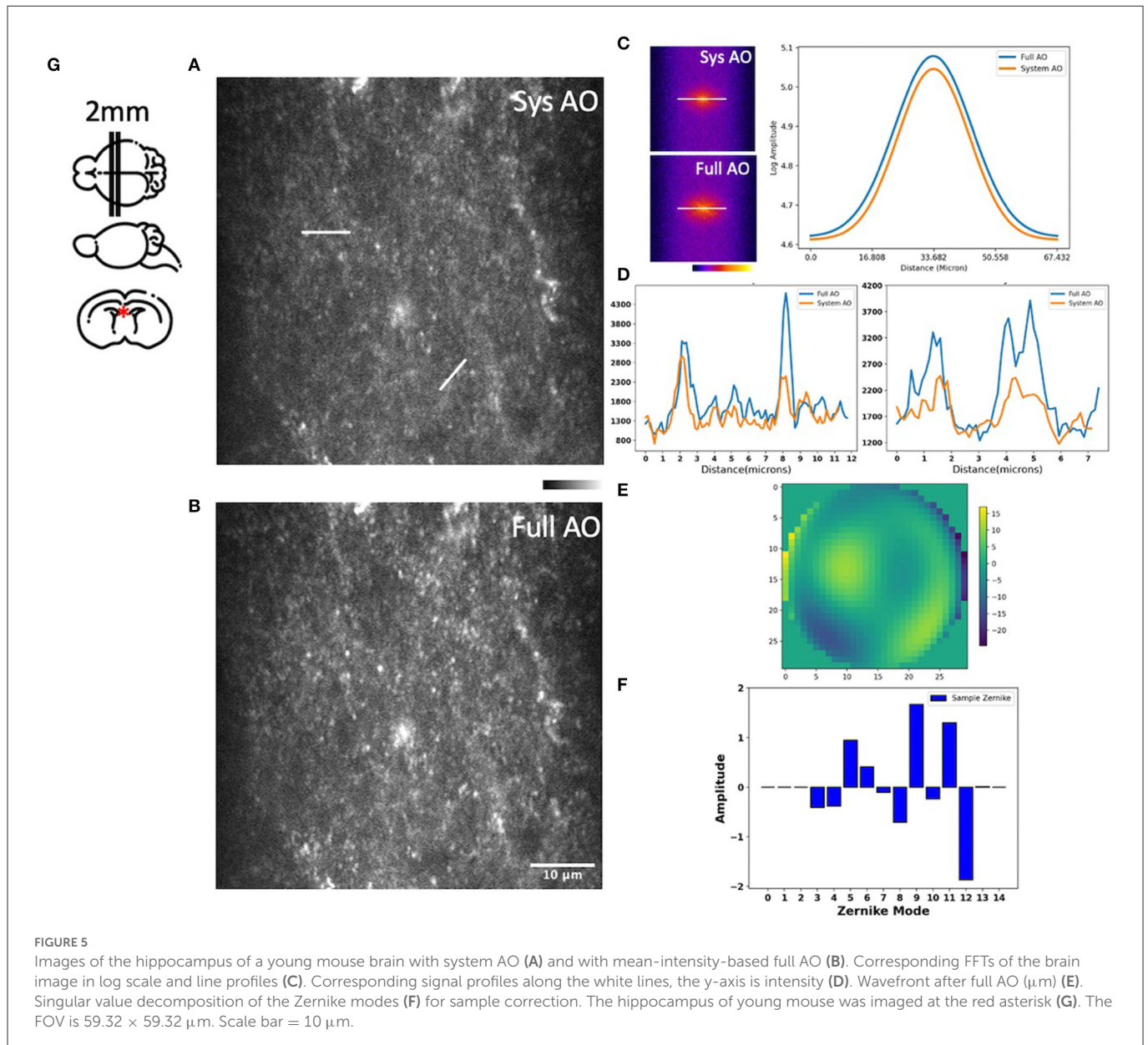
According to Figure 3B, although we are not getting improvement based on mean intensity, we achieve improvement based on max value, second moment, and Strehl ratio of PSF when the exposure time is larger than 0.5 s, with the percent changes between the uncorrected and corrected value reaching a constant soon after (Figure 3C). Therefore, we find that by performing our TPFM-AO approach at two distinct signal levels using mean or

max intensity of PSF when the improvement percentage of two of the measurements are almost the same, the sample correction has achieved its maximum improvement performance. In future work, we will further explore alternate correction metrics (e.g., second moment) for *in vivo* situations.

### 3. Results and discussion

#### 3.1. *In vitro* tissue mimic with AO correction for submicron bead imaging

We evaluated the experimental resolution improvement in a tissue phantom of the TPFM-AO microscope by measuring the full-width at half-maximum (FWHM) of the intensity profile of 0.2 μm beads embedded in a gel using a 960-nm laser excitation wavelength (Figure 4). Beads were embedded in a 5 mm thick 2% agarose gel and imaged at 50 μm depth (Figure 4A) to mimic a distorting tissue environment. We imaged the sample with system correction on, and then used a sensorless approach to compensate for the aberrations

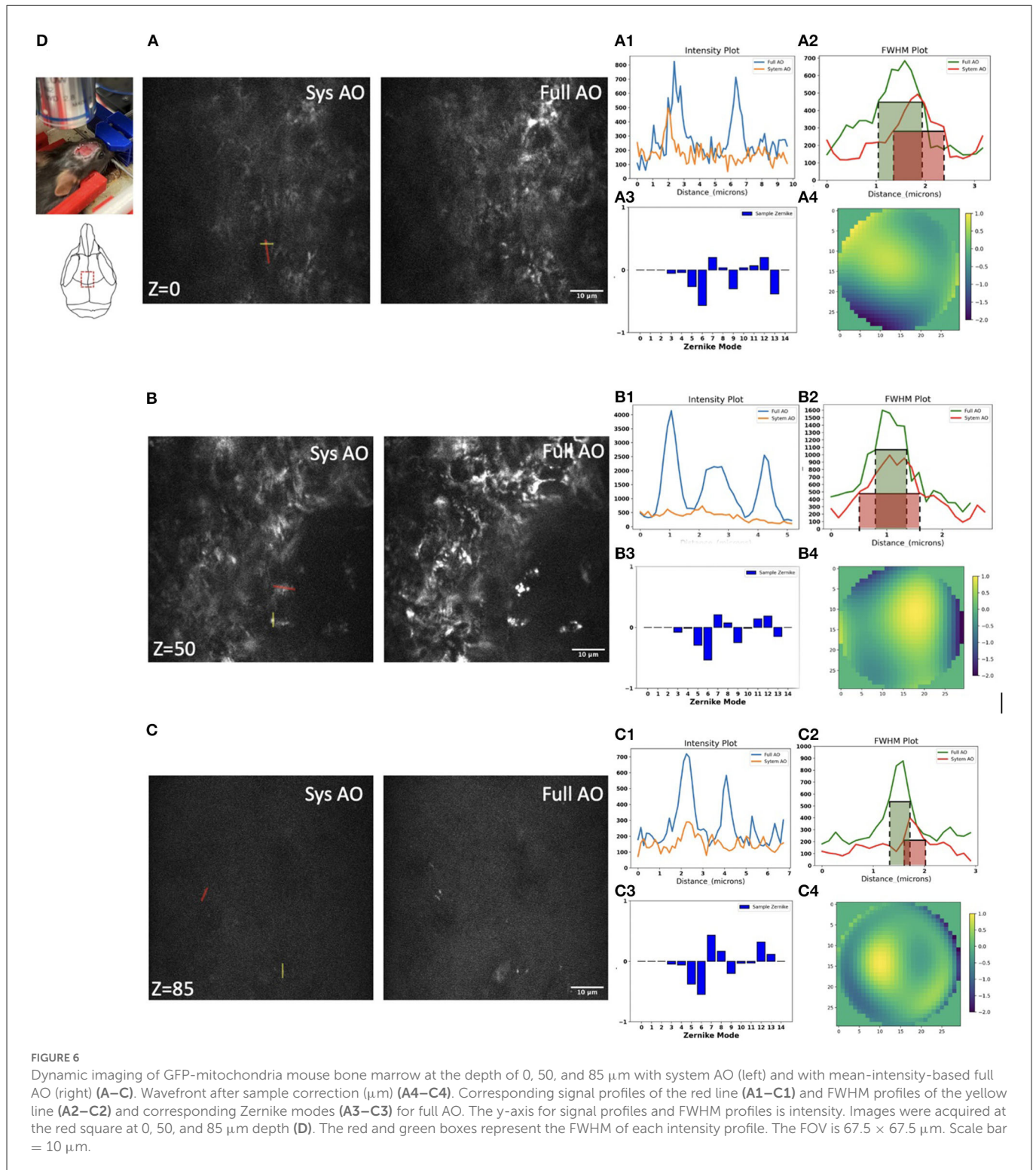


induced by the gel (Figure 4B). The full AO correction approach shows relatively high values of astigmatism (Z6) and coma (Z7) and yields the wavefront shown in Figures 4C, D. AO improved the full width at half maximum of the detected bead fluorescence with the average FWHM Gaussian fit of 10 measured  $0.2 \mu\text{m}$  radius 2-photon excited fluorescent beads improving from  $0.538 \pm 0.03 \mu\text{m}$  to  $0.408 \pm 0.03 \mu\text{m}$  after sample correction (Figure 4E).

### 3.2. AO correction enables high-resolution imaging of mitochondria organelle morphology in the mouse brain

We then measured and corrected aberrations for Dendra-2 mouse brain mitochondria using a 780 nm laser excitation

wavelength. Immediately after sacrifice, the mouse brain was cut into 2 mm thick slices, then embedded in 3% agarose to prevent movement. For imaging, the brain was immersed in phosphate buffered saline (PBS). Two photon fluorescence images were acquired in the hippocampal region, as indicated by a red asterisk in our brain diagram (Figure 5G). We found tissue wavefront distortions (Figure 5E) and aberrations due to the shape and high refractive index of the brain; mostly astigmatism (Z5, Z11), trefoil (Z9), and spherical (Z11) (Figure 5F). After AO, the images had improvements in mitochondrial intensity and sharpness laterally and, especially, axially by correcting the aberrations (Figures 5A, B). In the spatial frequency space (Figure 5C), the resolution improvement gained through aberration correction led to a substantial increase in the magnitude of high spatial frequency components, which indicates a sharper image with more fine detail. Signal profiles in the axial plane along the white lines show improved intensity (Figure 5D).

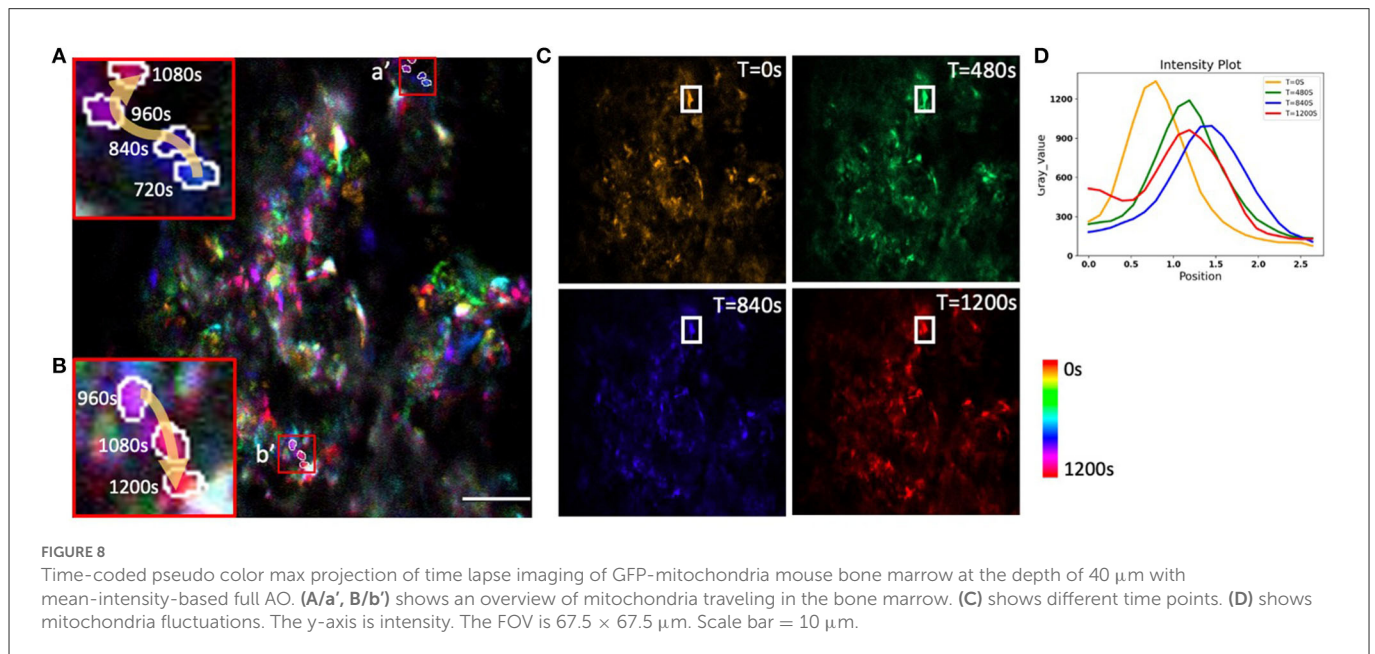
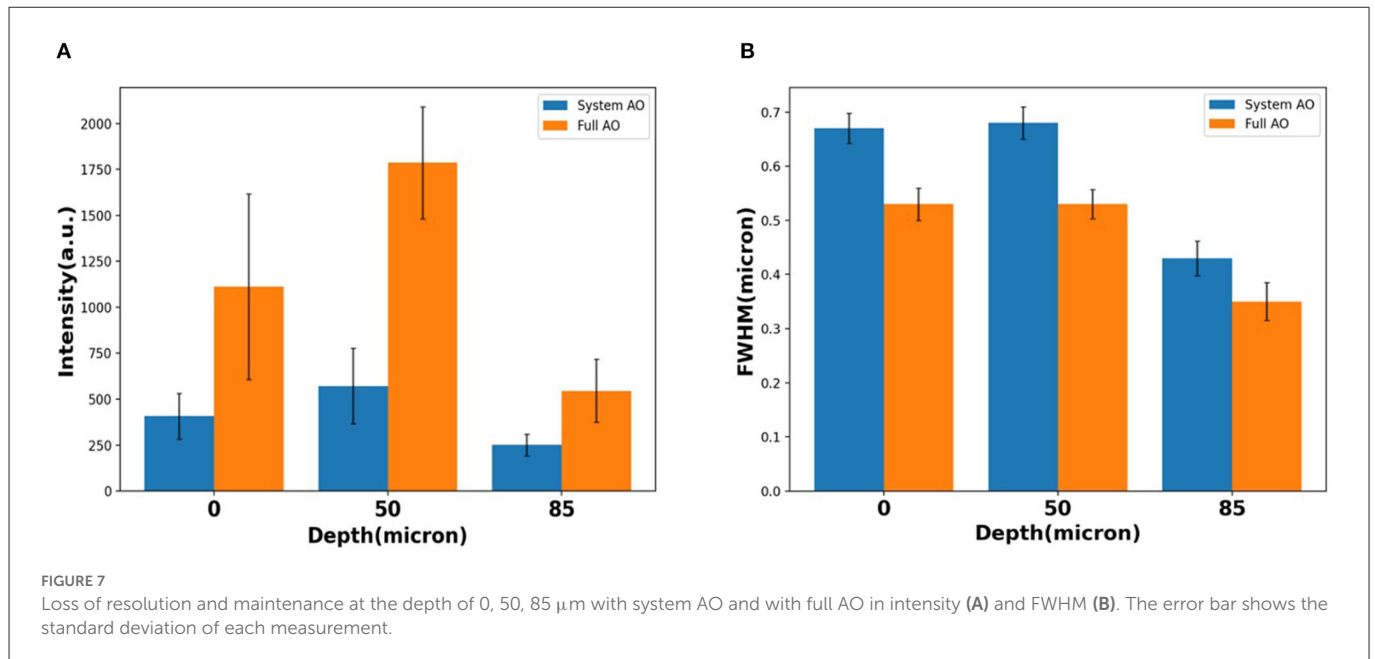


### 3.3. AO correction enables mitochondria imaging deep in mouse bone marrow *in vivo*

We next evaluated mitochondrial imaging through the outside layer of cranial bone into the bone marrow using the Dendra-2 mouse with 780 nm laser excitation wavelength. We evaluated 15 orders of Zernike modes to correct aberrations of the bone marrow *in vivo* because in preliminary experiments this achieved the best improvement of the PSF intensity and shape. We found

improvements in image intensity and resolution for *in vivo* TPF imaging of mitochondria in bone marrow at the depth of 0, 50, and 85  $\mu\text{m}$  (Figures 6A–C). Signal profiles along the red line show  $\sim 1.55\times$ ,  $\sim 3.58\times$ , and  $\sim 1.77\times$  intensity increases using sample AO correction at the depths of 0, 50, and 85  $\mu\text{m}$  separately (Figures 6A1–C1). The FWHM with full AO was enhanced by  $\sim 0.83\times$ ,  $\sim 0.74\times$  and  $\sim 0.9\times$  at the depth of 0, 50, and 85  $\mu\text{m}$  separately (Figures 6A2–C2). At the surface of the bone, we observed aberrations due to the shape and high refractive index of the bone; mostly astigmatism (Z6), trefoil





(Z9), and secondary astigmatism (Z13) (Figure 6A3). When we go 50  $\mu\text{m}$  deep in the bone marrow, the aberrations of primary astigmatism and trefoil are lower magnitude, but secondary astigmatism (Z13) remains (Figure 6B3). When we reach the opposite side of the bone marrow at a depth of 85  $\mu\text{m}$ , aberrations are mainly coma (Z7) and secondary astigmatism (Z13) resulting from the curved interior surface of the bone (Figure 6C3). The corrective wavefront after full AO is shown in Figures 6A4–C4.

When averaging across a whole image, the signal intensity showed  $\sim 2.73\times$ ,  $\sim 3.13\times$ , and  $\sim 2.18\times$  intensity increases over TPFM with system AO correction at 0, 50, and 85  $\mu\text{m}$  depth (Figure 7A). The average detected FWHM improvement was  $\sim 0.79\times$  ( $1.0 \mu\text{m}$  before and  $0.79 \mu\text{m}$  after),  $\sim 0.78\times$  ( $0.8 \mu\text{m}$  before and  $0.62 \mu\text{m}$  after), and  $\sim 0.81\times$  ( $0.45 \mu\text{m}$  before and  $0.36 \mu\text{m}$  after) at the depth of

0, 50, and 85  $\mu\text{m}$  respectively (Figure 7B). In order to evaluate the effect of AO on other emission wavelengths and confirm that the 85  $\mu\text{m}$  depth was through the bone marrow and into the bone on the other side, we captured second harmonic generation images with a bandpass filter of 390/18 (Supplementary Figure S2), finding that the FFT spectrum contains more high frequency information after full AO.

We also evaluated another multichannel dynamic *in vivo* bone marrow sample using the Dendra2 mitochondria mouse and co-labeling the blood vasculature using a rhodamine-B dextran conjugate. This stain required correction of the excitation beam using 840 nm excitation wavelength and emission with a 585/40 nm filter. We achieved improved imaging with full AO correction at three different depths of 30, 50, and 70  $\mu\text{m}$ , demonstrating the utility of

the system for AO in dynamic samples at multiple excitation and emission wavelengths (Supplementary Figure S3).

### 3.4. AO correction for dynamic mitochondria evaluation in mouse bone marrow

To evaluate the potential of AO correction to longitudinally monitor mitochondrial organelle dynamics in the bone, we corrected tissue aberration at a single plane 40  $\mu\text{m}$  deep in the bone marrow and then performed time lapse imaging for a total of 20 min (Supplementary Video S1). We quantified the temporal change in the cell mitochondria position (Figure 8) and observed differences in mitochondrial movement rates and trajectories (Figures 8A/a', B/b'). We found minimal intensity reduction over the imaging session, suggesting that there was little photobleaching or change in the tissue aberrations over 20 min (Figures 8C, D). A variety of cell and mitochondria trajectories are clearly present within relatively small regions of the bone marrow, which is not surprising given the high cellular density and diversity of cell types.

## 4. Conclusion

In summary, we calculated and corrected both the system aberrations and the sample aberrations caused by highly scattering brain tissue and bone with both a sensor-based approach using a Shack–Hartmann wavefront sensor and a sensorless AO approach using the PSF intensity as a metric. We demonstrate that low-order aberration correction provides a significant improvement when imaging through the bone into the living bone marrow. We find our TPFM-AO system increases the fluorescence intensity of the PSF and achieves fast imaging of subcellular organelles with  $\sim 400$  nm resolution. We also achieved close to a 2 fold increase in intensity and a reduction in PSF width using AO in living mouse bone marrow, allowing us to better characterize mitochondrial health and the survival of functioning cells. We also determined the criteria for stopping iterative sensorless AO correction, finding that once the improvement percentage of two measurements is near constant, sample correction has reached its best performance. This helps us more rapidly and efficiently correct the PSF. This AO approach could be used for the study of the dynamics of other organelles and is applicable to a wide range of biological tissues. In the future, we will further explore alternate correction metrics (e.g., second moment) for *in vivo* situations and use our system to study the transient functional responses in a cell population deep in the bone marrow previously unreachable by optical microscopy. This could transform MSC therapeutic approaches and enable new fundamental biological understanding in the musculoskeletal and neural fields.

## Data availability statement

The raw data supporting the conclusions of this article will be made available by the authors, without undue reservation.

## Ethics statement

The animal study was reviewed and approved by E.L. Rhodes Center for Animal and Dairy Science, Athens, GA.

## Author contributions

TZ was involved in conceptualization, design of the optical system, development of the algorithms and the LabView code, data analysis, project management, and writing. ARL was involved in conceptualization, design of the optical system, and project management. KFT was involved with the initial conceptualization, design of the optical system, and development of the algorithms and the LabView code. JAC was involved in investigation and writing. PAK and LJM were involved in conceptualization, investigation, and writing. All authors contributed to the article and approved the submitted version.

## Funding

This study was supported by National Science Foundation (1706916); National Institutes of Health (R21 Trailblazer #1R21EB027802-01); a Regenerative Engineering and Medicine Center seed grant; a Congressionally Directed Medical Research Program; and a Defense Medical Research and Development Program (W81XWH-20-1-0885).

## Conflict of interest

The authors declare that the research was conducted in the absence of any commercial or financial relationships that could be construed as a potential conflict of interest.

## Publisher's note

All claims expressed in this article are solely those of the authors and do not necessarily represent those of their affiliated organizations, or those of the publisher, the editors and the reviewers. Any product that may be evaluated in this article, or claim that may be made by its manufacturer, is not guaranteed or endorsed by the publisher.

## Supplementary material

The Supplementary Material for this article can be found online at: <https://www.frontiersin.org/articles/10.3389/fnimg.2023.959601/full#supplementary-material>

## References

- Albert, O., Sherman, L., Mourou, G., and Norris, T. B. (2000). Smart microscope: an adaptive optics learning system for aberration correction in multiphoton confocal microscopy. *Opt. Lett.* 25, 52–54. doi: 10.1364/OL.25.000052
- Andermann, M. L., and Kerlin, A. M. (2010). Chronic cellular imaging of mouse visual cortex during operant behavior and passive viewing. *Front. Cell. Neurosci.* 4, 3. doi: 10.3389/fncel.2010.00003
- Aviles-Espinosa, R., Andilla, J., Porcar-Guezenc, R., Olarte, O. E., Nieto, M., Levecq, X., et al. (2011). Measurement and correction of in vivo sample aberrations employing a nonlinear guide-star in two-photon excited fluorescence microscopy. *Biomed. Opt. Expr.* 2, 3135–3149. doi: 10.1364/BOE.2.003135
- Booth, M. J. (2006). Wave front sensor-less adaptive optics: a model-based approach using sphere packings. *Opt. Express* 14, 1339–1352. doi: 10.1364/OE.14.001339
- Callis, P. R. (1997). Two-photon-induced fluorescence. *Ann. Rev. Phys. Chem.* 48, 271–297. doi: 10.1146/annurev.physchem.48.1.271
- Calvo-Rodríguez, M., Hou, S. S., Snyder, A. C., Dujardin, S., Shirani, H., Nilsson, K. P. R., et al. (2019). In vivo detection of tau fibrils and amyloid  $\beta$  aggregates with luminescent conjugated oligothiophenes and multiphoton microscopy. *Acta Neuropathol. Commun.* 7, 171. doi: 10.1186/s40478-019-0832-1
- Chen, C., Qin, Z., He, S., Liu, S., Lau, S. F., Wu, W., et al. (2021). High-resolution two-photon transcranial imaging of brain using direct wavefront sensing. *Photon. Res.* 9, 1144–1156. doi: 10.1364/PRJ.420220
- Chen, Z., Ross, J. L., and Hambarzumyan, D. (2019). Intravital 2-photon imaging reveals distinct morphology and infiltrative properties of glioblastoma-associated macrophages. *Proc. Nat. Acad. Sci.* 116, 14254–14259. doi: 10.1073/pnas.1902366116
- Christodoulou, C., Spencer, J. A., Yeh, S. C. A., Turcotte, R., Kokkaliaris, K. D., Panero, R., et al. (2020). Live-animal imaging of native haematopoietic stem and progenitor cells. *Nature* 578, 278–283. doi: 10.1038/s41586-020-1971-z
- Débarre, D., Botcherby, E. J., Watanabe, T., Srinivas, S., and Booth, M. J. (2009). Image-based adaptive optics for two-photon microscopy. *Opt. Lett.* 34, 2495–2497. doi: 10.1364/OL.34.002495
- Denk, W., and Strickler, J. H. (1990). Two-photon laser scanning fluorescence microscopy. *Science* 248, 73–76. doi: 10.1126/science.2321027
- Diaspro, A., Bianchini, P., Vicidomini, G., Faretta, M., and Ramoino, P. (2006). Multi-photon excitation microscopy. *Biomed. Eng. Online* 5, 1–14. doi: 10.1186/1475-925X-5-36
- Folmes, C. D., Dzeja, P. P., and Nelson, T. J. (2012). Mitochondria in control of cell fate. *Circul. Res.* 110, 526–529. doi: 10.1161/RES.0b013e31824ae5c1
- Fried, H. U., Linnig, H. D., and Korsching, S. I. (2001). An inexpensive mouse headholder suitable for optical recordings. *Physiol. Behav.* 74, 253–255. doi: 10.1016/S0031-9384(01)00481-4
- Gropman, A. L. (2004). The neurological presentations of childhood and adult mitochondrial disease: established syndromes and phenotypic variations. *Mitochondrion*. 4, 503–520. doi: 10.1016/j.mito.2004.07.009
- Hell, S. (1992). Fundamental improvement of resolution with a 4Pi-confocal fluorescence microscope using two-photon excitation. *Opt. Commun.* 93, 277–282. doi: 10.1016/0030-4018(92)90185-T
- Hu, Y., Seker, B., Exner, C., Zhang, J., Plesnila, N., Schwarzaier, S. M., et al. (2021). Longitudinal characterization of blood-brain barrier permeability after experimental traumatic brain injury by in vivo 2-photon microscopy. *J. Neurotrauma*. 38, 399–410. doi: 10.1089/neu.2020.7271
- Itkin, T., Gur-Cohen, S., Spencer, J. A., Schajnovitz, A., Ramasamy, S. K., Kusumbe, A. P., et al. (2016). Distinct bone marrow blood vessels differentially regulate haematopoiesis. *Nature* 532, 323–328. doi: 10.1038/nature17624
- Jeong, D. C., and Tsai, P. S. (2013). All-optical osteotomy to create windows for transcranial imaging in mice. *Opt. Expr.* 21, 23160–23168. doi: 10.1364/OE.21.023160
- Kong, L. (2015a). In vivo neuroimaging through the highly scattering tissue via iterative multi-photon adaptive compensation technique. *Opt. Expr.* 23, 6145–6150. doi: 10.1364/OE.23.006145
- Kong, L. (2015b). In vivo deep tissue imaging via iterative multiphoton adaptive compensation technique. *IEEE J. Sel. Top. Quantum Electron.* 22, 40–49. doi: 10.1109/JSTQE.2015.2509947
- Kong, L., and Tang, J. (2016). Multicolor multiphoton in vivo imaging flow cytometry. *Opt. Expr.* 24, 6126–6135. doi: 10.1364/OE.24.006126
- Leuschner, F., Courties, G., Dutta, P., Mortensen, L. J., Gorbato, R., Sena, B., et al. (2015). Silencing of CCR2 in myocarditis. *Eur. Heart J.* 36, 1478–1488. doi: 10.1093/eurheartj/ehu225
- Li, Y., and Baran, U. (2014). Application of thinned-skull cranial window to mouse cerebral blood flow imaging using optical microangiography. *PLoS ONE* 9, e113658. doi: 10.1371/journal.pone.0113658
- Lo Celso, C., Fleming, H. E., Wu, J. W., Zhao, C. X., Miake-Lye, S., Fujisaki, J., et al. (2009). Live-animal tracking of individual haematopoietic stem/progenitor cells in their niche. *Nature* 457, 92–96. doi: 10.1038/nature07434
- Marsh, P. N., and Burns, D. (2003). Practical implementation of adaptive optics in multiphoton microscopy. *Opt. Expr.* 11, 1123–1130. doi: 10.1364/OE.11.001123
- Miao, F., Zhang, W., Sun, Y., Zhang, R., Liu, Y., Guo, F., and Yu, X. (2014). Novel fluorescent probes for highly selective two-photon imaging of mitochondria in living cells. *FEBS Lett.* 396, 7–13. doi: 10.1016/j.bios.2013.12.044
- Murphy, M. P. (2009). How mitochondria produce reactive oxygen species. *Biochem. J.* 417, 1–13. doi: 10.1042/BJ20081386
- Neil, M. A., Booth, M. J., and Wilson, T. (2000). Closed-loop aberration correction by use of a modal Zernike wave-front sensor. *Opt. Lett.* 25, 1083–1085. doi: 10.1364/OL.25.001083
- Noll, R. J. (1976). Zernike polynomials and atmospheric turbulence. *JOSA* 66, 207–211. doi: 10.1364/JOSA.66.000207
- Park, J. H., and Sun, W. (2015). High-resolution in vivo imaging of mouse brain through the intact skull. *Proc. Nat. Acad. Sci.* 112, 9236–9241. doi: 10.1073/pnas.1505939112
- Pham, A. H., McCaffery, J. M., and Chan, D. C. (2012). Mouse lines with photo-activatable mitochondria to study mitochondrial dynamics. *Genesis* 50, 833–843. doi: 10.1002/dvg.22050
- Pologruto, T. A., and Sabatini, B. L. (2003). ScanImage: flexible software for operating laser scanning microscopes. *Biomed. Eng.* 2, 1–9. doi: 10.1186/1475-925X-2-13
- Ricard, C. (2014). Six-color intravital two-photon imaging of brain tumors and their dynamic microenvironment. *Front. Cell. Neurosci.* 8, 57. doi: 10.3389/fncel.2014.00057
- Rueckel, M., and Mack-Bucher, J. A. (2006). Adaptive wavefront correction in two-photon microscopy using coherence-gated wavefront sensing. *Proc. Natl. Acad. Sci. U. S. A.* 103, 17137–17142. doi: 10.1073/pnas.0604791103
- Shi, L., Sordillo, L. A., Rodríguez-Contreras, A., and Alfano, R. (2016). Transmission in near-infrared optical windows for deep brain imaging. *J. Biophotonics*. 9, 38–43. doi: 10.1002/jbio.201500192
- Shih, A. Y., Driscoll, J. D., Drew, P. J., Nishimura, N., Schaffer, C. B., Kleinfeld, D., et al. (2012). Two-Photon Microscopy as a Tool to Study Blood Flow and Neurovascular Coupling in the Rodent Brain. *J. Cerebral Blood Flow Metab.* 32, 1277–1309. doi: 10.1038/jcbfm.2011.196
- Siegel, G. J., Albers, R. W., Agranoff, B. W., and Katzman, R. (1981). *Basic Neurochemistry*. Boston, MA, USA: Little Brown.
- Siesjo, B. K. (1978). *Brain Energy Metabolism*. New York, NY, USA: John Wiley and Sons.
- Sinefeld, D., Paudel, H. P., Ouzounov, D. G., and Bifano, T. G. (2015). Adaptive optics in multiphoton microscopy: comparison of two, three and four photon fluorescence. *Opt. Express* 23, 31472–31483. doi: 10.1364/OE.23.031472
- Southern, W. M., Nichenko, A. S., Tehrani, K. F., McGranahan, M. J., Krishnan, L., Qualls, A. E., et al. (2019). PGC-1 $\alpha$  overexpression partially rescues impaired oxidative and contractile pathophysiology following volumetric muscle loss injury. *Sci. Rep.* 9, 4079. doi: 10.1038/s41598-019-40606-6
- Spencer, J. A., Ferraro, F., Roussakis, E., Klein, A., Wu, J., Runnels, J. M., et al. (2014). Direct measurement of local oxygen concentration in the bone marrow of live animals. *Nature*. 508, 269–273. doi: 10.1038/nature13034
- Tao, X., Dean, Z., Chien, C., Azucena, O., and Bodington, D. (2013b). Shack-Hartmann wavefront sensing using interferometric focusing of light onto guide-stars. *Opt. Expr.* 21, 31282–31292. doi: 10.1364/OE.21.031282
- Tao, X., Norton, A., Kissel, M., and Azucena, O. (2013a). Adaptive optical two-photon microscopy using autofluorescent guide stars. *Opt. Lett.* 38, 5075–5078. doi: 10.1364/OL.38.005075
- Tehrani, K. F., Kner, P., and Mortensen, L. J. (2017a). Characterization of wavefront errors in mouse cranial bone using second-harmonic generation. *J. Biomed. Opt.* 22, 36012. doi: 10.1117/1.JBO.22.3.036012
- Tehrani, K. F., Kner, P., and Mortensen, L. J. (2019a). “Binary wavefront optimization for multi-photon intravital microscopy through intact cranial bone,” in *Adaptive Optics and Wavefront Control for Biological Systems V*, Vol. 10886 (SPIE), 1088605.
- Tehrani, K. F., Koukourakis, N., Czarske, J., and Mortensen, L. J. (2021). In situ measurement of the isoplanatic patch for imaging through intact bone. *J. Biophotonics*. 14, e202000160. doi: 10.1002/jbio.202000160
- Tehrani, K. F., Latchoumane, C. V., Southern, W. M., Pendleton, E. G., Maslesa, A., Karumbaiah, L., et al. (2019b). Five-dimensional two-photon volumetric microscopy of in-vivo dynamic activities using liquid lens remote focusing. *Biomed. Opt. Expr.* 10, 3591–3604. doi: 10.1364/BOE.10.003591
- Tehrani, K. F., Pendleton, E. G., Southern, W. M., Call, J. A., and Mortensen, L. J. (2017b). Two-photon deep-tissue spatially resolved mitochondrial imaging using membrane potential fluorescence fluctuations. *Biomed. Opt. Express*. 9, 254–259. doi: 10.1364/BOE.9.000254
- Turcotte, R., Alt, C., Runnels, J. M., Ito, K., Wu, J. W., Zaher, W., et al. (2017). Image-guided transplantation of single cells in the bone marrow of live animals. *Sci. Rep.* 7, 1–9. doi: 10.1038/s41598-017-02896-6

- Wang, K., Sun, W., Richie, C. T., Harvey, B. K., and Betzig, E. (2015). Direct wavefront sensing for high-resolution in vivo imaging in scattering tissue. *Nat. Commun.* 6, 7276. doi: 10.1038/ncomms8276
- Wang, M., Wu, C., Sinefeld, D., Li, B., and Xia, F. (2018). Comparing the effective attenuation lengths for long wavelength in vivo imaging of the mouse brain. *Biomed. Opt. Expr.* 9, 3534–3543. doi: 10.1364/BOE.9.003534
- Wilk, K., Yeh, S. C. A., Mortensen, L. J., Ghaffarigarakani, S., Lombardo, C. M., Bassir, S. H., et al. (2017). Postnatal calvarial skeletal stem cells expressing PRX1 reside exclusively in the calvarial sutures and are required for bone regeneration. *Stem Cell Rep.* 8, 933–946. doi: 10.1016/j.stemcr.2017.03.002
- Wright, A. J., Burns, D., Patterson, B. A., Poland, S. P., and Valentine, G. J. (2005). Exploration of the optimisation algorithms used in the implementation of adaptive optics in confocal and multiphoton microscopy. *Microsc. Res. Tech.* 67, 36–44. doi: 10.1002/jemt.20178
- Xu, C. (1996). Measurement of two-photon excitation cross sections of molecular fluorophores with data from 690 to 1050 nm. *J. Opt. Soc. Am. B* 13, 481–491. doi: 10.1364/JOSAB.13.000481
- Xu, Z., Zhang, D., He, X., and Huang, Y. (2016). Transport of Calcium Ions into Mitochondria. *Curr. Genom.* 17, 215–219. doi: 10.2174/1389202917666160202215748
- Yang, G., Pan, F., Chang, P. C., Gooden, F., and Gan, W. B. (2013). Transcranial two-photon imaging of synaptic structures in the cortex of awake head-restrained mice. *Methods Mol. Biol.* 1010, 35–43. doi: 10.1007/978-1-62703-411-1\_3
- Yang, W., Carrillo-Reid, L., Bando, Y., and Peterka, D. S. (2018). Simultaneous two-photon imaging and two-photon optogenetics of cortical circuits in three dimensions. *elife* 7, e32671. doi: 10.7554/eLife.32671.019
- Zhao, C. (2007). Orthonormal vector polynomials in a unit circle, Part I: basis set derived from gradients of Zernike polynomials. *Opt. Expr.* 15, 18014–18024. doi: 10.1364/OE.15.018014